

X-LineNet: Detecting Aircraft in Remote Sensing Images by a pair of Intersecting Line Segments

Haoran Wei^{a,b}, Wang Bing^{a,b}, Zhang Yue^b

^aUniversity of Chinese Academy of Sciences, Beijing, China

^bInstitute of Electrics, Chinese Academy of Sciences, Beijing, China

Abstract

In the field of aircraft detection, tremendous progress has been gained motivated by the development of deep convolution neural networks(DCNNs). At present, most state-of-art models based on DCNNs belong to top-down approaches which take a wide use of anchor mechanism. The obtaining of high accuracy in them relies on the enumeration of massive potential locations of objects with the form of rectangular bounding box, which is wasteful and less elaborate. In this paper, we present a novel aircraft detection model in a bottom-up manner, which formulated the task as detection of two intersecting line segments inside each target and grouping of them, thus we name it as *X-LineNet*. As the result of learning more delicate visual grammars information of aircraft, detection results with more concrete details and higher accuracy can be gained by *X-LineNet*. Just for these advantages, we designed a novel form of detection results—pentagonal mask which has less redundancy and can better represent airplanes than that of rectangular box in remote sensing images.

Keywords: Deep convolution neural network, Deep learning, Remote sensing images, Aircraft detection

1. Introduction

Driven by the rapid development of remote sensing technologies, remote sensing images with larger resolution and clearer texture can be easily accessed by the modern airborne and space borne sensors. In response to the demand for automatic analysis of remote sensing data, object detection has been widely researched, among which aircraft detection occupies an important part owing to the successful application in the field of military and air transportation. However, aircraft detection remains being a great challenge on account of the need for accurate and robust detection. Moreover, the complex background and noise, as well as the variation of spatial resolution of remote sensing images, weighting the difficulty of this task.

Conventional methods in aircraft detection mainly depends on manually engineered features. Cheng et al.[1], who develop a discriminatively trained model for extracting Histogram of Oriented Gradient (HOG)[2] feature pyramids from multiple scale, then threshold operation is performed on the response of the model to judge the presence of aircraft. Bai et al.[3], who select structural feature description as input of ranking Support Vector Machine(SVM)[4] to identify the existence of object. Besides, Rastegar et al.[5], who build an aircraft detection system in combine Wavelet features with SVM classifiers. Though these conventional methods are effective in specific scenes, the generalization capability of them need to be further improved in practice.

Inspired from the success of deep convolution neural networks (DCNNs)[6, 7], various methods based on DCNNs have been proposed in the research field of aircraft detection[8, 9, 10] which can automatically extract features through the back-

bone networks[11, 12], and the accuracy as well as robustness are greatly improved compared with manually engineered features. Most of these algorithms follow the principle of top-down detectors [13, 14, 15]. Cao et al.[10], who use selective search methods to generate a large set of region proposals, and then sending them into classifiers as well as modifying the final bounding boxes in a regression manner. Similarly, Ding et al.[8], who adopt a region proposal network[13] module to generate the proposals from a large set of anchor boxes[13], which are candidate boxes with fixed size densely distributed over the feature map. Although satisfactory results have been achieved by these top-down approaches, there are still some limits of them. First of all, this type of method convert aircraft detection into task of classifying rectangular regions, but the rectangular region is not an accurate representation for aircraft as there are some details are ignored, such as direction contexts of airplanes. Besides, the target of regression is the center point of the rectangular bounding box as well as its height and width which doesn't truly understand the aircraft's visual grammar information. Consequently, a large number of redundant bounding boxes may be generated and even may lead to false alarm uncontrollable. Third, these algorithms largely rely on anchor mechanism: In order to locate the targets with no omission, a large set of anchor boxes with different size and ratio are densely placed over the feature map. While only tiny set of boxes will have an overlap with ground truth, leading to the imbalance in positive and negative samples which slow down the training. Moreover, many hyperparameters are introduced related to anchors, such as sizes and aspect ratios of anchor boxes. All of these require a lot of prior knowledge to deploy.

Considering limits mentioned above in top-down approaches,

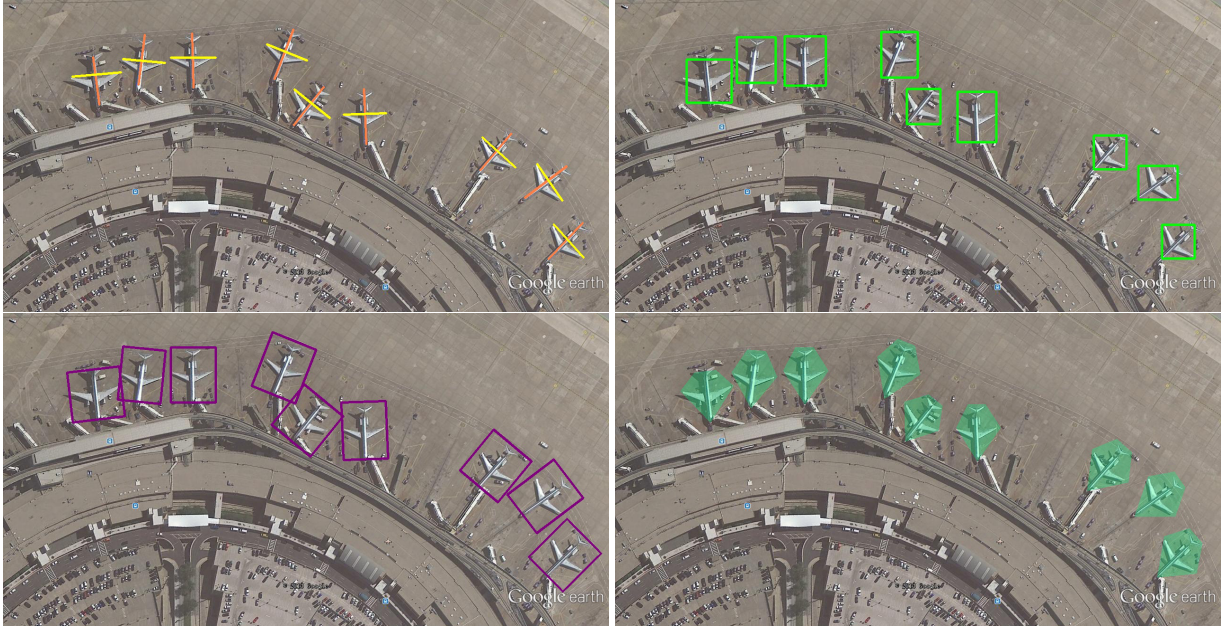


Figure 1: We predict a pair of line segments to obtain the aircraft’s bounding boxes. The left upper figure is the line segments inside the aircraft predicted by our model , the right upper figure is the horizontal bounding boxes, the left bottom one is the rotating bounding boxes, and the last one is the pentagonal mask.

inspired by Law’s work *CornerNet*[16] which detect objects via predicting and grouping paired corner points, we promote a bottom-up model *X-LineNet* to detect airplanes in this paper. We don’t carry on the method of points detection in *CornerNet* as it is not suitable for the task of aircraft detection in remote sensing images: single optical image may contains a large amount of airplanes which may frequently lead to errors of grouping points detected. Instead we formulate the task as detection of two line segments inside each aircraft and clustering of linear segments. These two set of target segments are defined as a pair of linear area from the head of the aircraft to the tail part as well as area between two airfoils. *X-LineNet* first predicts two heatmaps corresponding to two set of line segments respectively, and then groups these line segments according to their geometric relationships. As the result of dimension ascending from point to line, the difficulty of points grouping in *CornerNet* are solved. In addition, *X-LineNet* abandons the top-down detectors’[13, 14, 17, 18]anchor mechanism and successfully solved the problems mentioned above. A pair of interior segments in each aircraft provide more details information than a rectangular area, thus our model can output horizontal bounding boxes and rotating bounding boxes under a single network simultaneously. Additionally we propose pentagonal mask to be a new output form for *X-LineNet* to refine the position and direction information of each airplane target. Figure 1 illustrates these effects.

Our contributions and innovations are as follows:

(1).We promote a novel aircraft detection model which goes in a bottom-up manner and away with anchor mechanism. The feasibility of applying this new bottom-up method to the field of remote sensing is verified by us.

(2).We are the first to transform the task of airplane detection in remote sensing images to prediction and grouping of paired intersecting line segments. And detection results with more sophisticated contexts have been obtained by this way.

(3).In case of the problem of adhesion between aircraft in neighbor, a cutting algorithm is developed to separate the neighbor airplanes compulsively.

(4).Besides horizontal and rotating rectangular bounding boxes, one more accurate form of detection result can be generated within a single network simultaneously. That is the pentagonal mask form of prediction which contains less redundant context while more accurate localization.

The rest of the paper is organized as follows: In the next section, we introduce the related works done by researchers before and basic principle in our method. The details of our network and algorithms are shown in *Section 3*. We place our experiments results and analysis in *Section 4*. At last, our work is summarized and concluded in *Section 5*.

2. Related Works

2.1. Top-down aircraft detectors with anchors

Top-down frameworks based on anchor mechanism have dominated the field of aircraft detection[8, 9, 10] recently. Generally, these methods can be classified into two-stage detectors and one-stage detectors.

2.1.1. Two-stage detectors

Two-stage detectors decompose the task of detection into subtasks of generating region proposals and classifying of these candidate boxes. In the early *R-CNN*[19], region proposals are

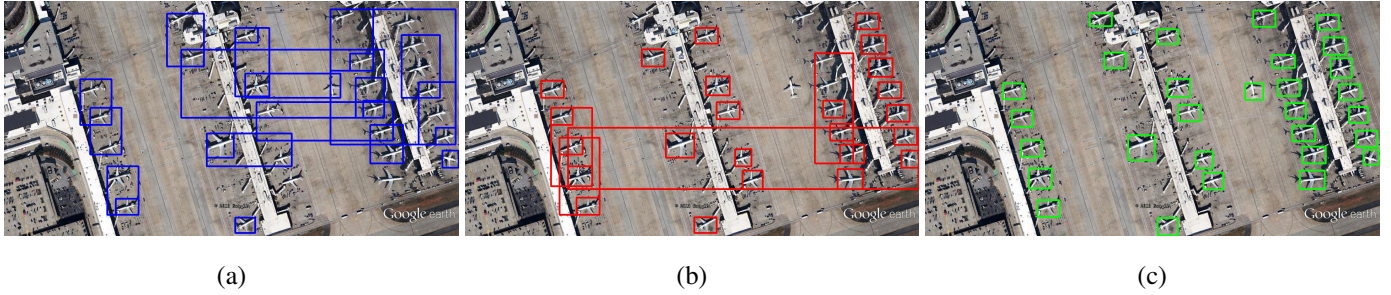


Figure 2: The figure (a) shows the CornerNet’s effect, figure (b) for ExtremeNet and figure (c) for X-LineNet.

produced under the algorithm of selective search, which can be quite inefficient as the generation of many redundant proposals. In order to lift the efficiency, *SPP*[20] and *Fast R-CNN*[21] designed a special pooling layer to improve it, but both of them are not end-end trainable. Later, a region proposal network(*RPN*)[13] were proposed in *Faster R-CNN*[13]. Mechanism of *RPN* can be illustrated in detail as below.

After the feature maps extracted by the backbone[11] from the original image, a large set of anchor boxes can be produced by densely placing rectangular boxes with different size and ratio. On account of filtering these numerous anchors, Non-Maximum Suppression(*NMS*) and scoring mechanism within *RPN*[13] are performed to generate the final regions of candidate. Final detection results can be accessed after the classification and modification of these proposals in parallel. Benefit from the adoption of *RPN*[13], the network can be trained end-to-end and accuracy of detection results greatly increased.

2.1.2. One-stage detectors

In pursuit of computation efficiency and inference speed, one-stage detectors get on detection within a single network away with region proposal module. Initially, *YOLOv1*[22] without anchor mechanism can’t provide accuracy comparable to that of two-stage detectors. Later, anchor methods are also extensively utilized in one-stage detectors[17, 14, 15] to improve the accuracy, massive anchors with different scales are densely placed within certain layers of the network.

Besides the gain in accuracy, there are some problems accompanied by the bringing in of anchor mechanism in one-stage detectors. First, a large set of anchors from multi scale can be produced to supply sufficient location information. While only a tiny set of them are positive samples with the overlap with ground truth above 0.7 or 0.5 typically. This phenomenon leads to the imbalance in positive and negative samples, which may prolong the process of training. Besides, many hyperparameters are introduced, for example, concrete settings for size and ratio of anchor boxes in certain layers, which bring in much inconvenience to adjust them carefully.

On account of drawbacks of anchor mechanism mentioned above, there has been many works on modifying it. In *RetinaNet*[15], *Focal Loss*[15] is promoted to avoid the issue of one-stage detector’s overwhelming by negative samples: In the process of generating anchors, weights are adjusted according to the distributions of samples. Furthermore, *MetaAnchor*[23]

is proposed to decrease the reliance of anchors’ settings on prior knowledge: Benefit from the subnetwork of anchor function generator, hyperparameters of anchor boxes can be learned dynamically and generalization of the model is greatly enhanced.

Our approach falls into category of one-stage detectors as the process of region proposal is discarded and accomplish the task of detection away with anchor mechanism. It is worth noting that the target space of searching is reduced from the $O(w^2h^2)$ to $O(wh)$ by abandoning anchors.

2.2. Bottom-up detectors based on DCNNs

In recent times, the research of detection in an *Anchor-Free* manner has become popular. *CornerNet* and *ExtremeNet* are two representative detectors of these new approaches. Their idea is to transform the object detection task into the process of predicting and grouping keypoints, which can be seen as detecting objects in a bottom-up way, and state-of-art results has been attained by them in *MS COCO*[24] benchmark. While it is not suitable to apply them to aircraft detection in remote sensing images for the reasons followed:

CornerNet’s[16] clustering algorithm draws on the method of Newell et al.[25], by embedding a vector on each corner points detected to group them. The basic assumption is that the distance (*Euclidean Distance*) between two corner points of the same object is small, and large between different objects. However, this process is not applicable to intensive occasions: With the large number of the same class objects densely distributed in a single image, such as remote sensing aircraft image, the algorithm has difficulty in converging and resulting in frequent embedding errors.

The grouping method of *ExtremeNet*[26] is to match 4 extreme points with the center point, and basic rules are based on the assumption that if geometric center points of 4 extreme points match the predicted center points then the same object should they belong to. However, this method is still unable to be applied to detect aircraft due to the fact that many of them may be spatially symmetric in remote sensing images.

Our model converts points detection to detection of line segments, which effectively solves the clustering problem that present bottom-up detectors have fallen into in the task of aircraft detection. Figure 2 shows a representative contrast result between *X-LineNet* and other two bottom-up detectors.

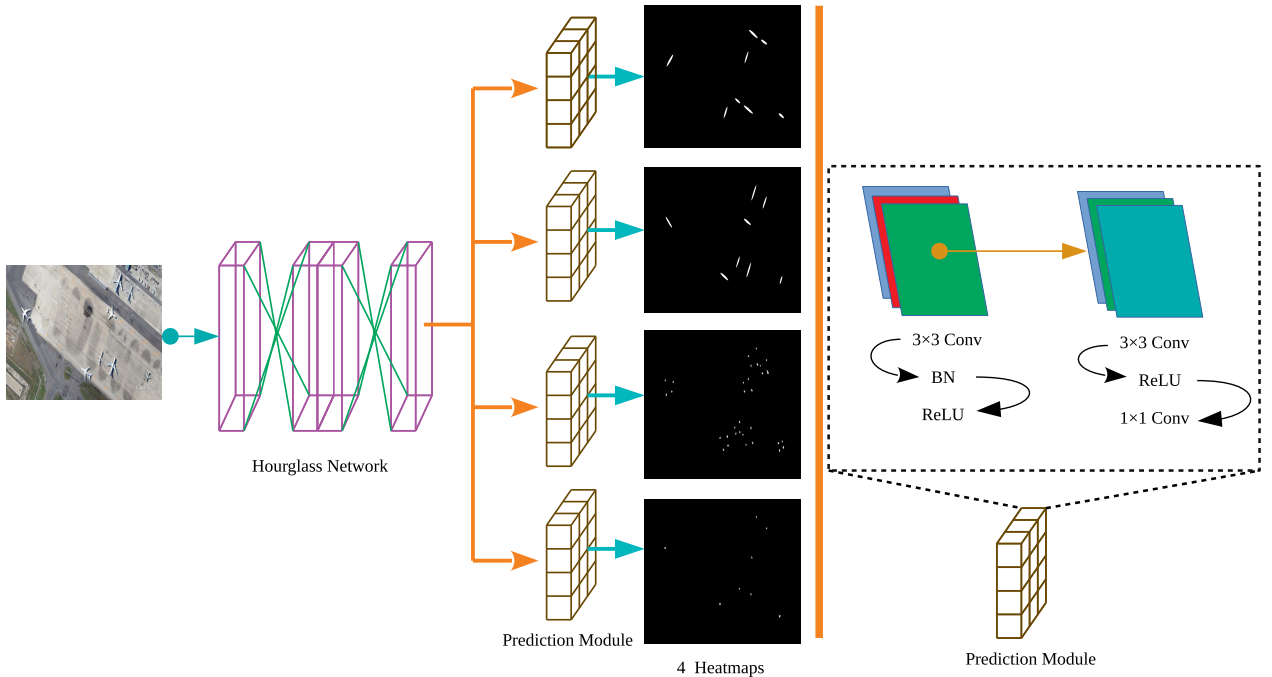


Figure 3: Illustration of our framework. The "Conv" is convolution layer, "BN" is Batch Normalization layer and "ReLU" is ReLU layer.

3. X-LineNet

3.1. Overview

X-LineNet detects each aircraft as a pair of segments which are defined as the line area from the head of the aircraft to the tail part as well as line area between two airfoils. 104-HourglassNetwork[27] is selected as the backbone of our model for the powerful capability of feature fusion. Four prediction modules in parallel after the backbone network are in charge of predicting four sets of heatmaps. The first two sets of heatmaps correspond to the detection of target line segments inside the aircraft respectively and each line segment display in the form of mask domain in them. On account of the issue of lines adhesion may occurred in detecting aircraft in neighbor, a third output terminal of heatmap is added for the prediction of four endpoints of two target line segments, which act as a basis for inspecting the phenomenon of adhesion and locate its position. Further more, in order to provide context of aircraft's direction, a fourth prediction module is designed to specify the concrete head position of aircraft. With these heatmaps provided, simple cutting and grouping algorithms are applied and finally three forms of bounding boxes can be generated by X-LineNet simultaneously. In this paper, we name these four heatmaps as heatmap A, B, C, D in order. Figure 3 shows an overview of our framework.

3.2. Detection of line segments and endpoints

Based on the feature map extracted by the backbone network, four sets of heatmaps will be generated in parallel after

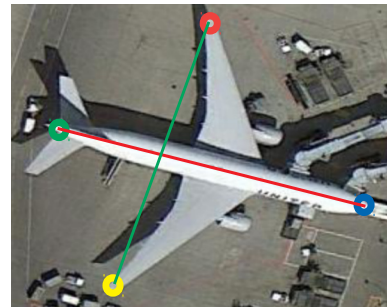


Figure 4: Keypoints and line segments. The blue, yellow, green and red points correspond to $(x_t, y_t), (x_l, y_l), (x_b, y_b), (x_r, y_r)$ respectively. The red segment is L_1 and the green one corresponds to L_2 .

a series of layers in prediction modules. Supposing the shape of the original input image is $H \times W$, the size of each heatmap is $\frac{H}{D} \times \frac{W}{D}$ where D corresponds to the output stride. Each pixel value $y \in [0, 1]^{\frac{H}{D} \times \frac{W}{D}}$ in heatmaps represents the confidence of being judged as positive sample.

As shown in Figure 4, let $(x_t, y_t), (x_l, y_l), (x_b, y_b), (x_r, y_r)$ be the concrete coordinates of four chosen keypoints inside each aircraft.

For heatmaps A and B , We define the segment from the head of one aircraft to the tail part as $L_1[(x_t, y_t), (x_b, y_b)]$, and $L_2[(x_l, y_l), (x_r, y_r)]$ as the segment between two airfoils. All pixels values within L_1 and L_2 set are fixed to the value of 1 as positive samples, and other pixels are regarded as the background

with their values setting to 0. In the process of training, objective function is set to the pixel-level logistic regression with a modified *Focal Loss*[15]:

$$L_{ls} = -\frac{1}{N} \sum_{i=1}^2 \sum_{xy} \begin{cases} (1 - V_{xy})^\gamma \log V_{xy}, & \text{if } V_{xy} = 1 \\ V_{xy}^\gamma \log(1 - V_{xy}), & \text{if } V_{xy} = 0 \end{cases} \quad (1)$$

where N is the number of aircraft, \hat{V} represents the pixel value at the coordinate (x, y) in heatmap A and B , and V corresponds to the ground truth. γ is a hyperparameter in original *Focal Loss*, here we set it to 2 in our experiments. Due to the fact that two sets of line segments are predicted separately, we add another \sum at the beginning of the formula.

The ground truth of the heatmap C is labeled as the four endpoints of two target line segments and act as the auxiliary information for inspecting the phenomenon of adhesion. The keypoints that lie in the head of aircraft are the targets to predict for the heatmap D which is responsible for providing angle information of each airplane in the process of generating pentagonal mask. Their corresponding loss L_{ep} and L_{kp} follow the same form of L_{ls} . And the total loss of our model can be expressed as :

$$Loss = \alpha L_{ls} + \beta L_{ep} + \gamma L_{kp} \quad (2)$$

where α is 1.2, and both β and γ are set to 0.8 in our experiments.

3.3. Cutting algorithm

The first stage of cutting algorithm is the inspection of adhesive segments and locate the adhesion position. First of all, 4-connected domains are generated in the heatmap C . Next minimum enclosing rectangle corresponding to each connected domain can be obtained. Then we introduce two relaxation conditions for the circumstance that there is only a single keypoint in one connected domain:

- (1). The area of the connected domain is not too large.
- (2). The shape of the connected domain is similar to that of a circle.

Supposing that \hat{H} and \hat{W} correspond to the height and width of each connected-domain's minimum enclosing rectangle respectively. The mathematical expressions of the relaxation conditions above are as follows:

$$\hat{W} \times \hat{H} < \alpha \quad \alpha \text{ is threshold 1} \quad (3)$$

$$\hat{H} \div \hat{W} < \beta \quad \beta \text{ is threshold 2} \quad (4)$$

Thus we can find out the connected domains that do not meet the relaxation conditions above, and there is a great probability that two keypoints contained in this area because of the fact that the distance between these two endpoints is too close.

The second stage of cutting algorithm is the compulsive separation of adhesive area. With the inspection of adhesion in the heatmap C , we cut in heatmap A and B with the centroid of these adhesion connected domains as the center point.

Algorithm 1 Cutting Algorithm.

```

1: let  $D$  be a collection of 4-connected domains in heatmap  $C$ 
2: for each  $d \in D$  do
3:   obtain the minimum external rectangle  $R$  of  $d$ ;
4:   let  $\hat{H}$  and  $\hat{W}$  be the length and width of  $R$ ;
5:   let  $p_c$  be the center point of  $R$ , and  $P$  is an array;
6:   let  $\alpha$  and  $\beta$  be two constant thresholds.
7:   if  $\hat{W} \times \hat{H} > \alpha$  or  $\hat{H} \div \hat{W} > \beta$  then
8:      $P \leftarrow p_c$ 
9:   end if
10: end for
11: for each  $p \in P$  in heatmap  $A$  and  $B$  do
12:   per pixel of  $L_a[(p_x - k, p_y), (p_x + k, p_y)] = 0$ 
13:   per pixel of  $L_b[(p_x, p_y - k), (p_x, p_y + k)] = 0$ 
14: end for

```

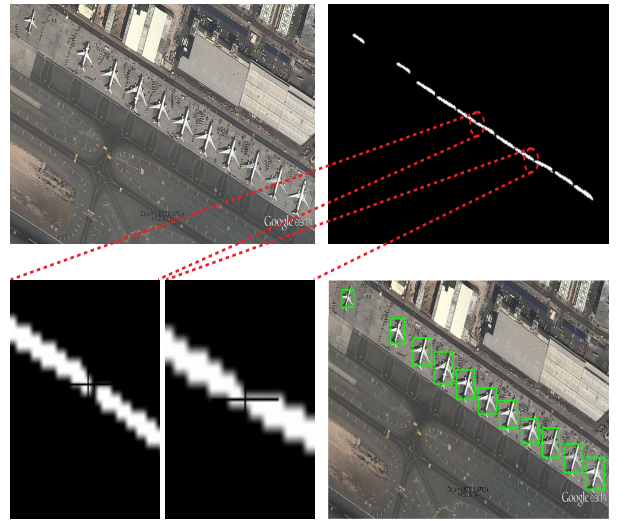


Figure 5: Illustration of Cutting Algorithm. The upper left figure represents the input image, and the upper right one is heatmap C after application of cutting algorithm. The last one shows the output result.

The specific method of cutting is to set k pixels to zero in both horizontal and vertical directions. Figure 5 shows its effect and Algorithm 1 shows this process. The k is 15, α is 200 and β is 1.5 in our model.

3.4. From heatmaps to line segments

After processing of these heatmaps obtained by the performing of cutting algorithm, issue of adhesion can be largely avoided. On account of the fact that each line segment we need maps a mask domain in the heatmap, a method based on ellipse-fitting algorithm is applied to extract target line segment in each mask. Concretely, an elliptical area can be obtained after fitting each 4-connected domain following the principles of least squares. We define the long axis of each ellipse as the desired segment.

3.5. The Generation of Bounding Boxes

X-LineNet can generate three forms of bounding boxes simultaneously. The process is illustrated as follows and its flow chart can be found in Figure 6.

3.5.1. Horizontal bounding boxes

The generation of horizontal bounding boxes are underway with the extraction of target line segments. Instead, we mapped the ellipse mask of each connected domain in heatmap A and B (Section 3.4) to two new maps, which act as a mechanism to filter the redundant area outside the ellipse region. Thus the final map of prediction can be obtained through superimposing of these two new maps. Simply find out the horizontal external rectangle of each 4-connected domain in the final one map, and then the horizontal bounding boxes can be gained. To avoid introducing new adhesion conditions in the process of superimposition, we set the edge pixels of each ellipse mask to 0 in each new map before it.

3.5.2. Rotating bounding boxes

Based on the collection of line segments obtained in Section 3.4, we group each pair of intersecting line segments which lie inside the same airplane by the following conditions:

- L_1 intersects with L_2 and the intersection roughly lies in the center of L_2
- The angle θ between L_1 and L_2 range in certain fields: $\theta \in [60^\circ, 120^\circ]$

Note that the definitions of L_1 and L_2 are the same as those mentioned in Section 3.2. After clustering of these line segments, the midpoint of the L_1 is defined as the center point of the rotating bounding box, the length of the L_1 and L_2 corresponds to the width and height of it respectively. Besides the angle between L_1 and the horizontal axis specify the rotation angle of it, thus the rotating bounding box can be obtained.

3.5.3. Pentagonal mask

During the generation of the rotating bounding box, we got four endpoints of each aircraft in the process of grouping line segments, but for the purpose of generating the pentagonal mask with extral direction context, we also need to know the specific meaning of these four endpoints. In order to achieve this aim we designed heatmap D , which in charge of providing the coordinate of head inside each aircraft, and then we match it to two endpoints of L_1 mentioned in Section 3.2. The matching degree is measured in *Euclidean distance*.

The endpoint with the largest matching value is regarded as the head point and the other one as the tail, thus other two keypoints of L_2 with specific position context inside the aircraft can be gained following the rotation of \vec{L}_1 , where the \vec{L}_1 is a vector from the tail to the head of each airplane. Due to the fact that the tail part of the aircraft actually take on in the form of line segment with certain length instead of point in the pentagonal mask. We extend the tail point to two endpoints of one segment following the direction parallel to L_2 , and the length of it are fixed as $\frac{1}{5}$ length of that in L_2 . With the specific definition of five points above, the pentagonal mask can be easily obtained.

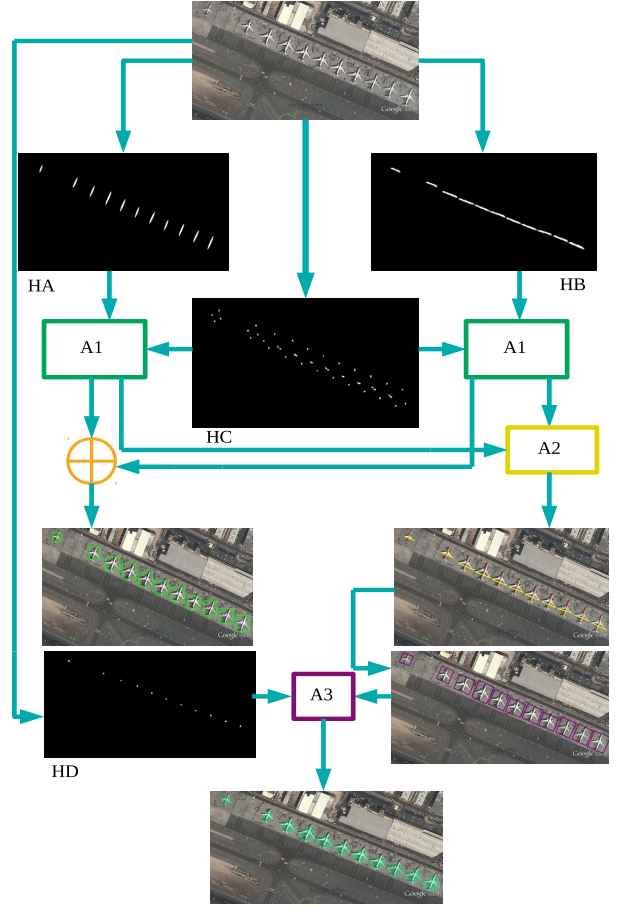


Figure 6: The Generation of Bounding Boxes. A1 is the cutting algorithm, A2 represents the process of line segments grouping, and A3 is the algorithm of generating pentagonal masks. HA, HB, HC HD are heatmap A, B, C, D.

4. Experiments

4.1. Preliminaries

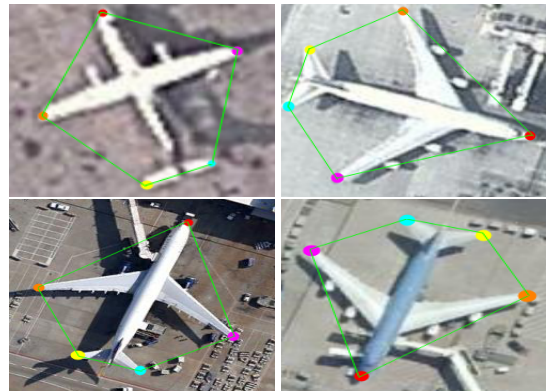


Figure 7: The label formats of Airplane-KP dataset.

Since there is no public dataset labeled in the form of aircraft's keypoints in remote sensing images, based on the public dataset UCAS-AOD[28], we produced a new dataset with

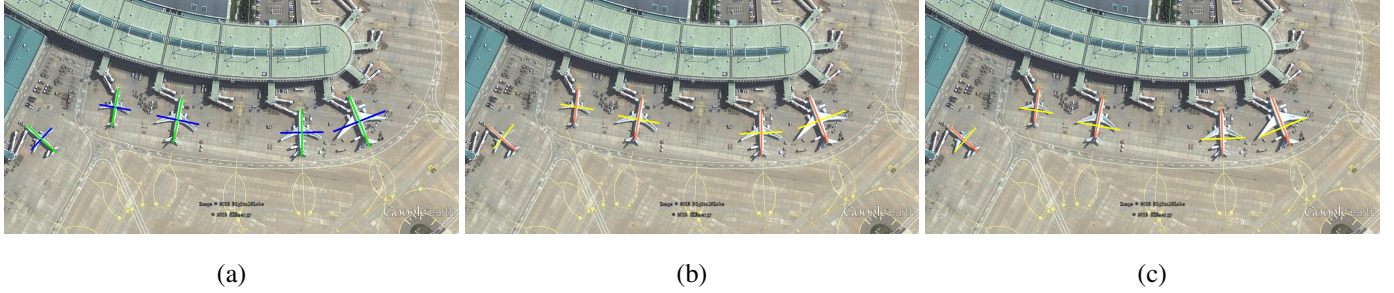


Figure 8: Figure (a) is the ground truth of train set converted from *UCAS-AOD* directly, figure (b) is the result trained with this train set, and figure (c) is trained by *Airplane-KP*.

keypoints inside each aircraft labeled. There are 7482 targets aircraft in 1000 images in *UCAS-AOD* totally. We randomly select 800 images used for training, leaving other 200 for testing. Each airplane in the train set are labeled as five keypoints along the anti-clockwise direction by us for better versatility. Concretely, these five endpoints are defined as following order: head of aircraft, left wing, left tail, right tail, right wing as shown in Figure 7. Note that we define the midpoint of both sides of the tail part as the tail point in our experiments. Besides, in order to test the generalization performance of *X-LineNet*, *NWPU VHR-10*[29] dataset are merged to our testing set, which contains about 700 aircraft in 80 images. All labels in test set are original in *UCAS-AOD* and *NWPU VHR-10*. Our dataset with keypoints labeled is named as *Airplane-KP* and available at <https://github.com/Ucas-HaoranWei>. All our experiments were performed on the *RTX-2080Ti GPU*, *19-9900K CPU* with *PyTorch 1.0*[30].

4.2. Training details

During the training phase, we set the input resolution to 511×511 and the output resolution to 128×128 following settings in *CornerNet*[16]. In order to get rid of the risk of overfitting, some data argumentation methods are applied, including random horizontal flipping, vertical flipping and color jitting and *PCA jitting*[7]. Adam[31] is selected as the optimizer for *X-LineNet* with learning rate of 0.0025. We trained our network from scratch for 40000 iterations with the batch size setting to 4.

4.3. Testing details

During stage of test, we preserved its original resolution for each input image. All of our test results are obtained from a single scale. In our experiments, we use the average precision (*AP*) as the evaluation metrics which are defined in *PASCAL VOC Challenge*[32]. We defined AP^1 as the test result on *UCAS-AOD*, AP^2 as the result on *NWPU VHR-10 dataset* and their average as AP^m . We used the default parameters in *PASCAL VOC* with *IoU*(Intersection over Union) which is 0.5 during testing.

4.4. Ablation studies

4.4.1. Cutting Algorithm in Adhesive Connected Domains

Cutting Algorithm (Section 3.3) gives a decent AP^m improvement of 1.4%. It effectively solve the issue of adjacent

segments which may occur in an occasion that aircraft are densely placed in a single image. As a result, accuracy get an effective ascension without introducing much cost of computation. Table 1 shows the contrast results.

Table 1: Comparisons of Cutting Algorithm.

| | AP^1 | AP^2 | AP^m |
|--------------|--------|--------|--------|
| no cutting | 91.2% | 90.7% | 90.9% |
| with cutting | 92.5% | 92.1% | 92.3% |

4.4.2. Comparisons with state-of-art frameworks

We compare *X-LineNet* with other state-of-art detectors used popularly in aircraft detection. Table 2 shows the contrast results. Our model with testing achieves an AP^m of 92.3%, outperforming all reported one-stage object detectors and goes far beyond other bottom-up models. *X-LineNet* is even competitive to the most advanced two-stage detectors. Noting that we only tested the rotating bounding boxes output by *X-LineNet* on *UCAS-AOD* for the lack of related labels in *NWPU VHR-10 dataset*. It is difficult to regress rotating bounding boxes in top-down detectors, we draw on a few detection models[33, 34] of text in natural scene to do this. Notable, *X-LineNet* improve about 2% AP^m compared with other top-down detectors with the method of rotating anchors or proposals to output rotating bounding boxes.

4.4.3. Comparison on different train set

X-LineNet can also be trained with the data converted from the original *UCAS-AOD* directly instead of *Airplane-KP* labeled by us. We define the two median lines of the original labeled rotating bounding box as the segments that need to be detected as shown in Figure 8. It is worth mentioning that our model can still achieve good accuracy with the converted train set. Table 3 shows the contrast results. *Airplane-KP* gives an AP^m improvement of 0.8% than the train data converted from *UCAS-AOD* directly by a code. Because the endpoints of segments in *Airplane-KP* are clearer which helps the cutting algorithm (Section 3.3) be implemented better.

Table 2: State-of-the-art comparisons. R means the outputs are rotating bounding boxes, S means single scale and M means multi-scale. The input size is the resolution fed into the model during training.

| Models | backbone | input size | AP^1 | AP^2 | AP^m |
|----------------------------|---------------|------------|--------------|--------------|--------------|
| Two-stage detectors | | | | | |
| Faster R-CNN[13] | vgg16 | 1200×600 | 86.4% | 85.2% | 87.4% |
| Faster R-CNN[12] | ResNet-50 | 1200×600 | 88.4% | 88.2% | 88.8% |
| Faster R-CNN[12] | ResNet-101 | 1200×600 | 89.8% | 90.4% | 90.1% |
| Faster R-CNN+FPN[35] | ResNet-101 | 1000×600 | 92.4% | 91.5% | 91.3% |
| Cascade R-CNN[36] | ResNet-101 | 1024×512 | 93.1% | 91.8% | 92.5% |
| Faster R-CNN+RRPN(R)[33] | ResNet-50 | 1000×600 | 90.4% | - | - |
| Faster R-CNN+R2CNN(R)[34] | ResNet-101 | 1000×600 | 90.9% | - | - |
| One-stage detectors | | | | | |
| YOLO9000[17] | DarkNet-19 | 544×544 | 82.4% | 81.4% | 81.9% |
| YOLOv3[18] | DarkNet-53 | 608×608 | 85.4% | 85.5% | 85.4% |
| SSD[14] | ResNet-101 | 513×513 | 88.7% | 89.4% | 89.0% |
| RetinaNet[15] | ResNet-101 | 512×512 | 89.8% | 90.9% | 90.3% |
| ConerNet(S)[16] | 104-Hourglass | 511×511 | 76.2% | 77.4% | 76.8% |
| ConerNet(M)[16] | 104-Hourglass | 511×511 | 76.8% | 77.4% | 77.1% |
| ExtremeNet[26] | 104-Hourglass | 511×511 | 78.3% | 77.2% | 77.7% |
| Our(H) | 104-Hourglass | 511×511 | 92.5% | 92.1% | 92.3% |
| Our(R) | 104-Hourglass | 511×511 | 92.8% | - | - |

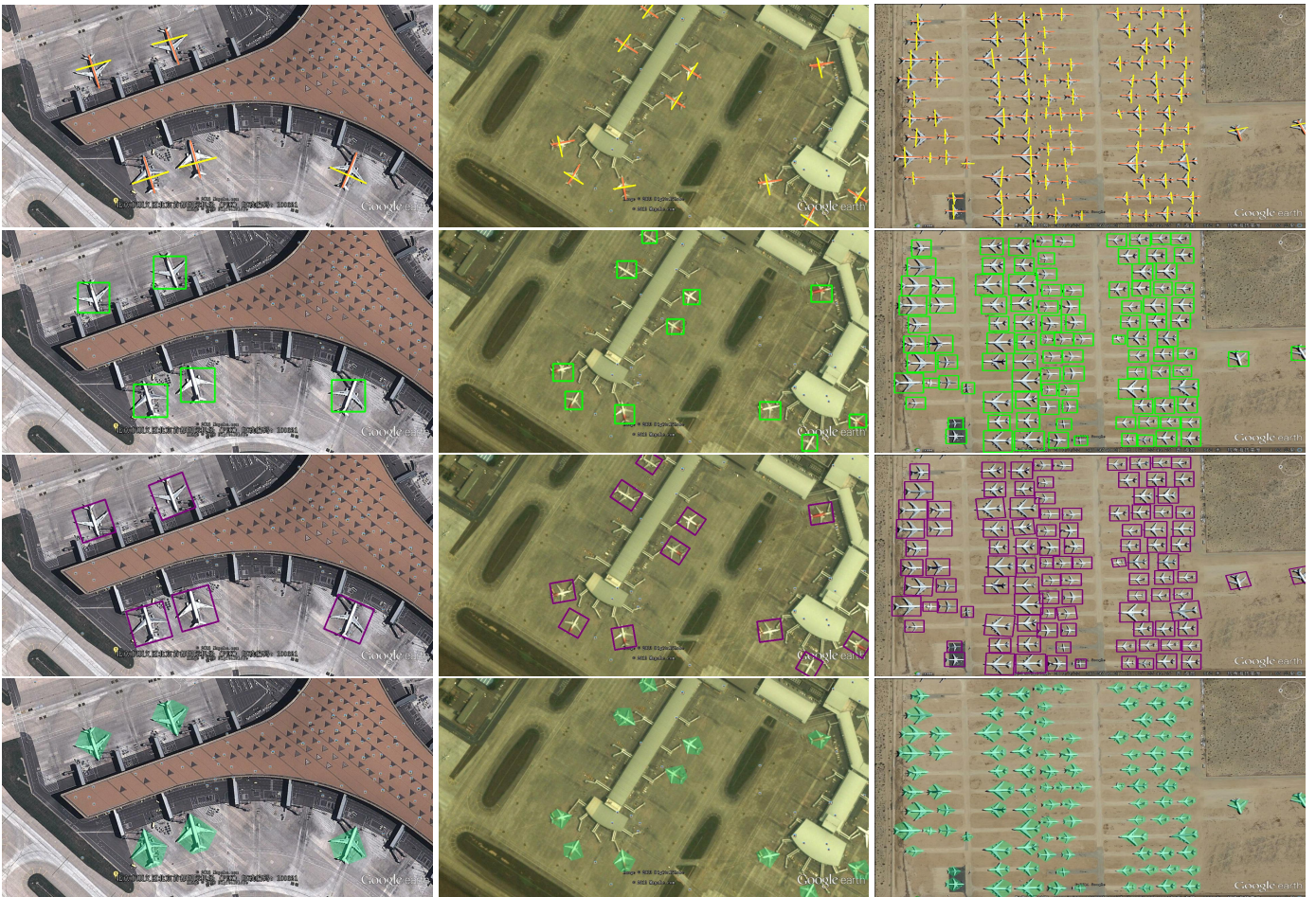


Figure 9: Qualitative results output by X-LineNet.

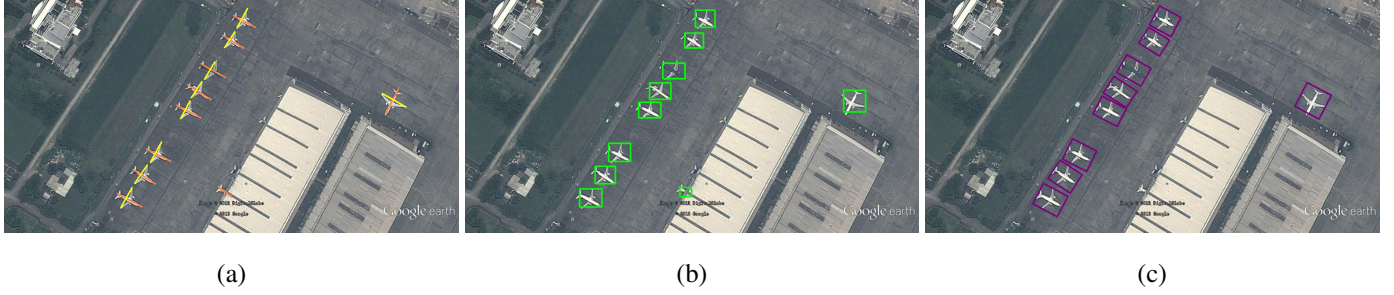


Figure 10: The leaking plane tail underneath the image is detected by X-LineNet, and is shown in the figure (a). Since there is no other line segment to group with it, it is not shown in figure (c).

Table 3: Comparisons on different train set.

| | AP^1 | AP^2 | AP^m |
|---------------------|--------|--------|--------|
| converted train set | 91.9% | 91.2% | 91.5% |
| <i>Airplane-KP</i> | 92.5% | 92.1% | 92.3% |

4.4.4. Error analysis

X-LineNet has three forms of detection results. The pentagonal mask box is a refinement of the rotation bounding box and they are gained from the grouping of line segments. Unfortunately, due to the lack of relevant datasets, we did not test it in experiments. The horizontal bounding box doesn't use segment clustering, so its accuracy is a little different from that of rotation box.

Because our network enhances the learning of target's visual grammar, the airplane can still be detected in an occasion that it is severely shielded or not fully displayed at the edge of the image with no label provided in our test set which may lead to "false alarm". This situation can be mitigated by the process of line segments clustering like Figure 10 shows. In addition, for small targets, due to the line segment domain is too small in heatmaps, its fitting ellipse is closer to a circle, which may result in a long axis extraction error (*Section 3.2*) and lead to omission in the process of generating rotation boxes. Those are the reasons why these two form of outputs have a tiny gap in Table 2.

5. Conclusion

In conclusion, we present a novel model to detect aircraft in remote sensing images based on a bottom-up method. We switch the task of aircraft detection into detection of line segments and prove that the bottom-up detection method is still competitive compared with the top-down method in the field of remoting sensing airplane detection.

References

- [1] G. Cheng, J. Han, L. Guo, X. Qian, P. Zhou, X. Yao, X. Hu, Object detection in remote sensing imagery using a discriminatively trained mixture model, *ISPRS Journal of Photogrammetry and Remote Sensing* 85 (2013) 32–43.
- [2] N. Dalal, B. Triggs, Histograms of oriented gradients for human detection, in: *International Conference on computer vision & Pattern Recognition (CVPR'05)*, Vol. 1, IEEE Computer Society, 2005, pp. 886–893.
- [3] X. Bai, H. Zhang, J. Zhou, Vhr object detection based on structural feature extraction and query expansion, *IEEE Transactions on Geoscience and Remote Sensing* 52 (10) (2014) 6508–6520.
- [4] C. Cortes, V. Vapnik, Support-vector networks, *Machine learning* 20 (3) (1995) 273–297.
- [5] S. Rastegar, A. Babaeian, M. Bandarabadi, Y. Toopchi, Airplane detection and tracking using wavelet features and svm classifier, in: *2009 41st Southeastern Symposium on System Theory*, IEEE, 2009, pp. 64–67.
- [6] Y. LeCun, L. Bottou, Y. Bengio, P. Haffner, et al., Gradient-based learning applied to document recognition, *Proceedings of the IEEE* 86 (11) (1998) 2278–2324.
- [7] A. Krizhevsky, I. Sutskever, G. E. Hinton, Imagenet classification with deep convolutional neural networks, in: *Advances in neural information processing systems*, 2012, pp. 1097–1105.
- [8] P. Ding, Y. Zhang, W.-J. Deng, P. Jia, A. Kuijper, A light and faster regional convolutional neural network for object detection in optical remote sensing images, *ISPRS journal of photogrammetry and remote sensing* 141 (2018) 208–218.
- [9] F. Zhang, B. Du, L. Zhang, M. Xu, Weakly supervised learning based on coupled convolutional neural networks for aircraft detection, *IEEE Transactions on Geoscience and Remote Sensing* 54 (9) (2016) 5553–5563.
- [10] Y. Cao, X. Niu, Y. Dou, Region-based convolutional neural networks for object detection in very high resolution remote sensing images, in: *2016 12th International Conference on Natural Computation, Fuzzy Systems and Knowledge Discovery (ICNC-FSKD)*, IEEE, 2016, pp. 548–554.
- [11] K. Simonyan, A. Zisserman, Very deep convolutional networks for large-scale image recognition, *arXiv preprint arXiv:1409.1556*.
- [12] K. He, X. Zhang, S. Ren, J. Sun, Deep residual learning for image recognition, in: *Proceedings of the IEEE conference on computer vision and pattern recognition*, 2016, pp. 770–778.
- [13] S. Ren, K. He, R. Girshick, J. Sun, Faster r-cnn: Towards real-time object detection with region proposal networks, in: *Advances in neural information processing systems*, 2015, pp. 91–99.
- [14] W. Liu, D. Anguelov, D. Erhan, C. Szegedy, S. Reed, C.-Y. Fu, A. C. Berg, Ssd: Single shot multibox detector, in: *European conference on computer vision*, Springer, 2016, pp. 21–37.
- [15] T.-Y. Lin, P. Goyal, R. Girshick, K. He, P. Dollár, Focal loss for dense object detection, in: *Proceedings of the IEEE international conference on computer vision*, 2017, pp. 2980–2988.
- [16] H. Law, J. Deng, Cornernet: Detecting objects as paired keypoints, in: *Proceedings of the European Conference on Computer Vision (ECCV)*, 2018, pp. 734–750.
- [17] J. Redmon, A. Farhadi, Yolo9000: better, faster, stronger, in: *Proceedings of the IEEE conference on computer vision and pattern recognition*, 2017, pp. 7263–7271.
- [18] J. Redmon, A. Farhadi, Yolov3: An incremental improvement, *arXiv preprint arXiv:1804.02767*.
- [19] R. Girshick, J. Donahue, T. Darrell, J. Malik, Rich feature hierarchies for accurate object detection and semantic segmentation, in: *Proceedings of the IEEE conference on computer vision and pattern recognition*, 2014, pp. 580–587.

- [20] K. He, X. Zhang, S. Ren, J. Sun, Spatial pyramid pooling in deep convolutional networks for visual recognition, *IEEE transactions on pattern analysis and machine intelligence* 37 (9) (2015) 1904–1916.
- [21] R. Girshick, Fast r-cnn, in: *Proceedings of the IEEE international conference on computer vision*, 2015, pp. 1440–1448.
- [22] J. Redmon, S. Divvala, R. Girshick, A. Farhadi, You only look once: Unified, real-time object detection, in: *Proceedings of the IEEE conference on computer vision and pattern recognition*, 2016, pp. 779–788.
- [23] T. Yang, X. Zhang, Z. Li, W. Zhang, J. Sun, Metaanchor: Learning to detect objects with customized anchors, in: *Advances in Neural Information Processing Systems*, 2018, pp. 320–330.
- [24] T.-Y. Lin, M. Maire, S. Belongie, J. Hays, P. Perona, D. Ramanan, P. Dollár, C. L. Zitnick, Microsoft coco: Common objects in context, in: *European conference on computer vision*, Springer, 2014, pp. 740–755.
- [25] A. Newell, Z. Huang, J. Deng, Associative embedding: End-to-end learning for joint detection and grouping, in: *Advances in Neural Information Processing Systems*, 2017, pp. 2277–2287.
- [26] X. Zhou, J. Zhuo, P. Krähenbühl, Bottom-up object detection by grouping extreme and center points, *arXiv preprint arXiv:1901.08043*.
- [27] A. Newell, K. Yang, J. Deng, Stacked hourglass networks for human pose estimation, in: *European Conference on Computer Vision*, Springer, 2016, pp. 483–499.
- [28] H. Zhu, X. Chen, W. Dai, K. Fu, Q. Ye, J. Jiao, Orientation robust object detection in aerial images using deep convolutional neural network, in: *2015 IEEE International Conference on Image Processing (ICIP)*, IEEE, 2015, pp. 3735–3739.
- [29] G. Cheng, P. Zhou, J. Han, Learning rotation-invariant convolutional neural networks for object detection in vhr optical remote sensing images, *IEEE Transactions on Geoscience and Remote Sensing* 54 (12) (2016) 7405–7415.
- [30] A. Paszke, S. Gross, S. Chintala, G. Chanan, E. Yang, Z. DeVito, Z. Lin, A. Desmaison, L. Antiga, A. Lerer, Automatic differentiation in pytorch.
- [31] D. P. Kingma, J. Ba, Adam: A method for stochastic optimization, *arXiv preprint arXiv:1412.6980*.
- [32] M. Everingham, L. Van Gool, C. K. Williams, J. Winn, A. Zisserman, The pascal visual object classes (voc) challenge, *International journal of computer vision* 88 (2) (2010) 303–338.
- [33] J. Ma, W. Shao, H. Ye, L. Wang, H. Wang, Y. Zheng, X. Xue, Arbitrary-oriented scene text detection via rotation proposals, *IEEE Transactions on Multimedia* 20 (11) (2018) 3111–3122.
- [34] Y. Jiang, X. Zhu, X. Wang, S. Yang, W. Li, H. Wang, P. Fu, Z. Luo, R2cnn: Rotational region cnn for orientation robust scene text detection, *arXiv preprint arXiv:1706.09579*.
- [35] T.-Y. Lin, P. Dollár, R. Girshick, K. He, B. Hariharan, S. Belongie, Feature pyramid networks for object detection, in: *Proceedings of the IEEE Conference on Computer Vision and Pattern Recognition*, 2017, pp. 2117–2125.
- [36] Z. Cai, N. Vasconcelos, Cascade r-cnn: Delving into high quality object detection, in: *Proceedings of the IEEE Conference on Computer Vision and Pattern Recognition*, 2018, pp. 6154–6162.